# Auxiliary master equation approach within stochastic wave functions: Application to the interacting resonant level model

Max E. Sorantin,[*] Delia M. Fugger, Antonius Dorda, Wolfgang von der Linden, and Enrico Arrigoni[†]

*Institute of Theoretical and Computational Physics, Graz University of Technology, 8010 Graz, Austria*

We present further developments of the auxiliary master equation approach (AMEA), a numerical method to simulate many-body quantum systems in as well as out of equilibrium and apply it to the interacting resonant level model to benchmark the new developments. In particular, our results are obtained by employing the stochastic wave functions method to solve the auxiliary open quantum system arising within AMEA. This development allows us to reach extremely low wall times for the calculation of correlation functions with respect to previous implementations of AMEA. An additional significant improvement is obtained by extrapolating a series of results obtained by increasing the number of auxiliary bath sites, $N_B$, used within the auxiliary open quantum system formally to the limit of $N_B \to \infty$. Results for the current-voltage characteristics and for equilibrium correlation functions are compared with the one obtained by exact and matrix-product states–based approaches. Further, we complement this benchmark by the presentation of spectral functions for higher temperatures where we find different behaviors around zero frequency depending on the hybridization strength.

## I. INTRODUCTION

Quantum impurity models have a long history in many-body quantum mechanics. Some prominent examples include the single impurity Anderson model [1] (SIAM), the (Anderson-) Holstein model [2], the Kondo model [3], and the interacting resonant level model [4] (IRLM). They feature interesting, unconventional physics such as the Kondo effect [5] or negative differential conductance [6] and allow for experimental in terms of quantum dots [7]. Besides this, the solution of quantum impurity problems alone constitutes already a crucial task in dynamical mean-field theory [8].

Since the late 2000s, there has been increasing interest in quantum impurities out of equilibrium and the development of numerical methods which are able to accurately simulate such systems poses a great challenge for contemporary condensed matter theory. Existing methods [9] include iterated perturbation theory [10], numerical renormalization group [11], real-time quantum Monte Carlo (QMC) [12,13], noncrossing approximation and beyond [14,15], imaginary-time QMC supplemented by a double analytical continuation [16–19], scattering-states approaches [20,21], perturbative and renormalization group (RG) methods [22–25], time-dependent density-matrix RG and related tensor-network approaches [26–28], numerical RG [29], flow equation [30], functional RG [31,32], and dual fermions [33,34]. A method developed over the past few years is the so-called auxiliary master equation approach [35–37] (AMEA). The advantage of this approach is that, in contrast to approaches which simulate a closed Hamiltonian system, it allows us to directly address the steady state. Also time-dependent correlation functions can be readily evaluated starting from the steady state or any arbitrary initial condition.

AMEA is based on mapping the physical system to an auxiliary open quantum system of Lindblad form. The dynamics of the resulting auxiliary system is described by the density matrix and is solved by numerical means. In previous works the Lindblad system was solved by using the so-called superfermion (SF) representation [38], which formulates the superoperator problem in terms of a standard operator problem with twice as many sites. The operator problem was then solved by standard numerical many-body techniques such as Krylov-space methods [36,39] (ED) or time evolution with matrix product states [40] (MPS). AMEA within SF+MPS was successfully used to calculate highly accurate spectral functions of the SIAM under the influence of a bias voltage [40,41] and the SF+ED implementation was employed as impurity solver within single-site steady-state nonequilibrium dynamical mean-field theory [42–45] (DMFT).

In equilibrium, the combination of density functional theory (DFT) with DMFT (DFT+DMFT) has proven to be very successful in describing materials with strong correlations [46]. However, to address real materials one often has to consider multiorbital correlated regions. Accordingly, on the technical side, for DFT+DMFT one needs a multiorbital impurity solver, which is modeled by an interconnected impurity consisting of multiple interacting sites in contact with individual baths. Within existing implementations of AMEA, SF+MPS, and SF+ED, as well as other nonperturbative nonequilibrium approaches, the treatment of such multiple interacting sites has limitations related either to the memory (SF+ED) or to the CPU time (SF+MPS). For this reason, a different approach to solve the many-body Lindblad problem

————
[*]sorantin@tugraz.at
[†]arrigoni@tugraz.at

is needed in order to employ AMEA as an impurity solver for nonequilibrium DFT+DMFT.

In this work, we make a step in this direction and test an alternative approach which does not rely on the SF representation, namely stochastic wave functions [47–49] (SWF). The new method is statistical in nature and most notably highly parallelizable. This makes it a very promising candidate to exploit the multicore architecture of (future-) cluster facilities. In addition, we introduce the notion of finite-size scaling within AMEA and report on progress regarding the optimization problem arising when mapping to the auxiliary system.

To test and benchmark the new developments, we apply AMEA to the IRLM where we can compare to the existing literature. In addition, we present a short study of the spectral function in dependence of temperature. Our results show the development of a central peak at higher temperatures which rises (lowers) its amplitude for increasing temperature depending on the hybridization strength. This work is structured as follows.

We begin by describing the technical aspects in Secs. II–IV and present the results for the IRLM in Sec. V. In more detail, in Sec. II we outline AMEA for spinless one-dimensional systems and discuss the size limits of existing AMEA approaches with respect to DMFT. Section III and the Appendix are devoted to the description of the SWF algorithm; the finite-size scaling is introduced in Sec. IV. In Sec. V we apply AMEA within SWF to the IRLM and test the finite-size scaling scheme and the capability to compute correlation functions against the literature. We also discuss the temperature dependence of the impurity spectral function. Finally, we present our conclusions together with a summary and outlook in Sec. VI.

## II. AUXILIARY MASTER EQUATION APPROACH

We briefly review AMEA to deal with fermionic impurity problems. We consider a generic interacting region of size $N_{\text{int}}$ connected to a left and right baths of noninteracting fermions. Accordingly, we write the Hamiltonian as

$$H = H_{\text{int}} + H_{\text{Baths}} + H_{\text{Hyb}}. \tag{1}$$

Here $H_{\text{int}}$ describes the interacting region, $H_{\text{Baths}} = \sum_{\alpha=L/R} H_{B_\alpha}$ corresponds to the remaining reservoirs, and $H_{\text{Hyb}}$ contains the hopping terms connecting the baths to the interacting region. In the following we will assume that an individual bath is connected only to a single site of the interacting region.

The idea of AMEA is to model the physical situation by an auxiliary open quantum system described by the Lindblad equation. It consists of the interacting region and additional bath sites to approximate the action of the leftover Hamiltonian on the interacting region. In more detail, the Lindblad superoperator (Liouvillian) defining the dynamics of the open quantum system of size $L = N_{\text{int}} + 2N_B$ reads [50]

$$\mathcal{L}\rho = -i[H_{\text{int}}, \rho] + \mathcal{L}_D\rho, \tag{2}$$

$$\mathcal{L}_D\rho = \sum_{\alpha=L/R} \mathcal{L}_\alpha\rho, \tag{3}$$

where $\rho$ is the density matrix of the Lindblad system. The Liouvillian of the dissipative bath sites is given by

$$\begin{aligned}
\mathcal{L}_\alpha\rho = &-i\sum_{ij} E_{ij}^{(\alpha)}[c_i^\dagger c_j, \rho] \\
&+ 2\sum_{ij} \Gamma_{ij}^{(\alpha),(1)}\left(c_j\rho c_i^\dagger - \frac{1}{2}\{\rho, c_i^\dagger c_j\}\right) \\
&+ 2\sum_{ij} \Gamma_{ij}^{(\alpha),(2)}\left(c_i^\dagger\rho c_j - \frac{1}{2}\{\rho, c_j c_i^\dagger\}\right), \tag{4}
\end{aligned}$$

where $\alpha$ denotes the left (right) reservoir [51] and $c_i^{(\dagger)}$ are the creation (annihilation) operators of a fermion on site $i$ of the open quantum system. The time evolution of the system is described by the Lindblad equation,

$$\frac{d}{dt}\rho(t) = \mathcal{L}\rho(t). \tag{5}$$

For the steady state of the original system, Eq. (16), the Dyson equation for the interacting region in the formulation of Keldysh Green's functions reads

$$\underline{\mathbf{G}}_{\text{int}}^{-1}(\omega) = \underline{\mathbf{g}}_{0,\text{int}}^{-1}(\omega) - \underline{\boldsymbol{\Delta}}_{\text{ph}}(\omega) - \underline{\boldsymbol{\Sigma}}(\omega), \tag{6}$$

where an underline indicates the 2×2 Keldysh matrix,

$$\underline{\mathbf{X}} \equiv \begin{pmatrix} \mathbf{X}^{\text{Ret}} & \mathbf{X}^{\text{Kel}} \\ \mathbf{0} & \mathbf{X}^{\text{Adv}} \end{pmatrix}, \tag{7}$$

and bold denotes the matrix structure in site indices, $\mathbf{X} = X_{ij}$. In Eq. (6) $\underline{\mathbf{g}}_{0,\text{int}}$ is the Green's function (GF) of the interacting region when isolated from the baths and without interaction, $\underline{\boldsymbol{\Sigma}}$ is the self-energy, holding all the information about the interaction, and $\underline{\boldsymbol{\Delta}}$ is the so-called hybridization describing the effect of $H_{\text{Baths}} + H_{\text{Hyb}}$ on the interacting region. For the present case in which the first (last) site of the interacting region couple to the left (right) bath, the hybridization has the spatial structure $\underline{\boldsymbol{\Delta}} = \text{diag}[\underline{\Delta}_{\text{ph}}^{(L)}, 0, \ldots, 0, \underline{\Delta}_{\text{ph}}^{(R)}]$.

The mapping from the physical to the auxiliary system is performed by fitting the parameters $E^\alpha$, $\Gamma^{\alpha,(1,2)}$ in Eq. (4) such that the hybridization in the auxiliary system approximates the physical hybridization as close as possible, $\underline{\Delta}_{\text{aux}}^{(\alpha)} \approx \underline{\Delta}_{\text{ph}}^{(\alpha)}$, and this is the only approximation made within AMEA. The accuracy of the mapping can then be systematically improved by increasing the number of auxiliary bath sites $N_B$ and it becomes formally exact in the limit of $N_B \to \infty$. Once the mapping is performed, one can solve the auxiliary system by some appropriate numerical method and evaluate observables belonging to the interacting region. Their accuracy in describing the corresponding exact quantities will be directly related to the difference between $\underline{\Delta}_{\text{aux}}^{(\alpha)}$ and $\underline{\Delta}_{\text{ph}}^{(\alpha)}$.

### A. Different AMEA implementations and their applicability to multiorbital DMFT

Here we want to briefly discuss the applicability of the different AMEA implementations as impurity solvers within multiorbital DMFT.

To address the open quantum system problem described by Eq. (4), one can use the SF representation or the SWF approach presented in this paper. These two approaches can

in turn be combined with two different schemes to carry out the time evolution, namely ED or MPS. This makes a total of four different combinations (SF+ED [36], SF+MPS [40], SWF+ED, present paper, and SWF+MPS).

To estimate the number of correlated orbitals that can be treated within DMFT for each one of these methods, we assume that at least four bath sites are needed per correlated orbital to represent accurately a single bath [37,52] leading to a total system size of $L = N_{\mathrm{imp}}(N_B + 1)$. SF+ED is limited in system size to $L \leqslant 7$ due to memory requirements. It is, thus, restricted to the treatment of a single correlated orbital. With the same memory limits, SWF+ED allows for a twice-as-large system, $L \leqslant 14$, which accommodates two correlated orbitals. One should, however, point out that, for the same $L$, SWF+ED requires more CPU resources. On the other hand, the wall time [53] can be reduced considerably due to the high parallelizability of the SWF approach.

When using MPS as a time-evolution algorithm for AMEA, the situation is more complex. On the one hand, MPS is generically not limited in system size but rather expensive with respect to the wall time. On the other hand, conventional MPS becomes inefficient when the system is not truly one dimensional. This is the case in the SF representation, where the impurity+bath system is mapped into a ladder structure [36,40]. Also the inclusion of additional correlated orbitals makes the problem higher dimensional and thus unsuitable for MPS. Recently, a generalization of MPS suitable to address efficiently a multiorbital impurity problem, the so-called fork tensor product states [54,55] (FTPS) approach, has been introduced. This approach, implemented within the SWF representation, could constitute a promising candidate for a nonequilibrium multiorbital DMFT impurity solver.

### B. Mapping to the auxiliary system

Here we briefly want to summarize the mapping procedure and mention key points that we need for the present work. For a thorough discussion of the mapping and technical details we refer to our previous work [37]. The mapping is performed for each individual bath $\alpha$ by minimizing a suitable cost function,

$$\chi^2(\boldsymbol{x}_\alpha) \equiv \chi_\alpha^2 = \int \left\| \underline{\Delta}_{\mathrm{ph}}^{(\alpha)} - \underline{\Delta}_{\mathrm{aux}}^{(\alpha)} \right\|^2 d\omega,$$

$$\left\| \underline{\Delta}_{\mathrm{ph}}^{(\alpha)} - \underline{\Delta}_{\mathrm{aux}}^{(\alpha)} \right\|^2 \equiv \sum_{\xi \in \{\mathrm{Ret,Kel}\}} \left[ \mathrm{Im}\Delta_{\mathrm{ph}}^{(\alpha),\xi}(\omega) \right.$$
$$\left. - \mathrm{Im}\Delta_{\mathrm{aux}}^{(\alpha),\xi}(\omega; \boldsymbol{x}_\alpha) \right]^2. \quad (8)$$

Here we have introduced a parameter vector $\boldsymbol{x}_\alpha$ that parametrizes the matrices $E^\alpha$, $\Gamma^{\alpha,(1,2)}$ in Eq. (4), from which one evaluates the auxiliary hybridization $\Delta_{\mathrm{aux}}^{(\alpha)}$. It is important to note that the precise form of the cost function is very flexible and may be chosen differently for different physical situations. However, proper cost functions should quantify how well the auxiliary system captures some desired physical situation. For instance, the quadratic deviation as used in Eq. (8). One important property of the mapping is that proper cost functions decrease exponentially with the number of fit parameters [37], $-\log \chi_\alpha \propto \dim(\boldsymbol{x}_\alpha)$, which typically leads to a rapid increase of accuracy when the number of bath sites $N_B$ is increased.

In previous works, Eq. (8) was minimized via a parallel tempering (PT) algorithm which is appropriate to find the global minimum. However, it should be noted that within AMEA it is not strictly necessary to find the global optimum [56]. In general, the fit struggles to resolve sharp features such as band edges in the retarded component or the Fermi jumps in the Keldysh component at zero temperature. Therefore, $T = 0$ cannot be reached exactly in practice and the auxiliary system always has some nonzero effective temperature.

#### *Developments of the fit*

With increasing dimensionality of the fitting problem, the PT algorithm gets computationally prohibitive and it is not able to find even good local minima anymore for [57] $\dim(\boldsymbol{x}) = 2N_B(N_B + 1) \gtrsim 80$. Good minima should be such that they display an exponential decrease in the cost function when the number of bath sites is increased. To obtain good-enough minima for $N_B = 7, 8$, we use the fact, which we observed empirically, that the $\Gamma$ matrices of obtained minima typically have very low rank. Utilizing a variable rank parametrization in terms of a corresponding matrix $\gamma$,

$$\gamma = (\vec{\gamma}_1, \ldots, \vec{\gamma}_{\mathrm{rank}_\gamma}), \quad \Gamma = \gamma \gamma^\dagger, \quad (9)$$

where $\vec{\gamma}_i$ denote column vectors of length $L$. Note that the maximal useful rank typically increases with the system size [58]. With this procedure, we have reduced the dimensionality of the parameter vector to $\dim(\boldsymbol{x}) = 2N_B(\mathrm{rank}_\gamma + 1)$, extending the applicability of the PT algorithm to about $N_B = 8$. To achieve an exponential decrease in the cost function for even more bath sites we have adopted an optimization algorithm which makes use of the gradient of the cost function, which can be evaluated directly. This information is not used in the PT algorithm. Suitable gradient-based approaches can be found in the area of machine learning, which provides algorithms tailored to find local minima in very high dimensional problems utilizing variants of steepest descent. Here we employ the ADAM [59] optimizer as implemented in the python library tensorflow [60].

Steepest descent approaches are obviously very sensitive to the starting point. In our case, it has proven to be very effective to first find the solution for a small auxiliary system (small $N_B$) and, consequently, add bath sites until the required $N_B$ is reached. For a fixed $N_B$, we start with the result of the previous system size and increase the rank stepwise until no significant decrease in the cost function is observed. In addition to being applicable for larger $N_B$, the ADAM routine is also faster than PT for a given $N_B$. This is because the PT algorithm tries to explore the total phase space, whereas ADAM only follows a certain path.

### III. SOLUTION OF THE LINDBLAD SYSTEM WITH STOCHASTIC WAVE FUNCTIONS

The auxiliary open system is still correlated but due to its finite size can be addressed by numerical techniques. One route is to make use of the so-called SF representation [38], which maps a superoperator problem to a standard, albeit non-Hermitian, operator problem. The drawback of this approach is that the resulting SF problem is formulated on twice as many effective sites leading to a rapid increase in the

numerical complexity. In previous works employing AMEA we have successfully used the SF representation together with established many-body techniques such as Krylov-space methods [35,36] or MPS [40] to solve for steady-state properties. A completely different route is to use SWF [47–49], also referred to as "quantum jumps," to solve the auxiliary many-body problem. The method is based on the stochastic nature of the Lindblad problem and is formulated in terms of wave functions instead of a density matrix and thus circumvents the need to square the Hilbert space. In the following, we will only give a brief introduction to the SWF method and focus more on a practical prescription to simulate the many-body Lindblad system arising within AMEA. For more details, mathematical definitions and background we refer to the literature [47–49]. In the following we consider a Lindblad system of spinless fermions of size $L$.

The density operator $\rho(t)$ can be mapped onto a probability distribution $P[\vec{\psi}, t]$ for the quantum mechanical (many-body) wave function [61],

$$|\psi\rangle = \sum_{\lambda=1}^{2^L} \psi_\lambda |\lambda\rangle,$$

$$\vec{\psi} \equiv (\psi_1, \dots, \psi_{2^L}), \tag{10}$$

where $\lambda$ indexes a complete set of (many-body) basis states [62]. With the Hilbert space volume element,

$$D\vec{\psi} D\vec{\psi}^* \equiv \prod_{\lambda=1}^{2^L} \frac{i}{2} d\psi_\lambda d\psi_\lambda^*, \tag{11}$$

defining the needed probability measure [63], the expectation value of an observable can then be formally expressed as

$$\langle A(t) \rangle = \int D\vec{\psi} D\vec{\psi}^* \langle \psi | A | \psi \rangle P[\vec{\psi}, t]. \tag{12}$$

In short, instead of dealing with an evolution equation for the density matrix, one formulates a stochastic process on the Hilbert space. For the specific case of a Lindblad system, the process is simulated according to a stochastic differential equation leading to the algorithm presented in Fig. 1.

In this algorithm, a state vector $|\psi\rangle$ is evolved in time according to an effective, but non-Hermitian, Hamiltonian, $H_{\text{eff}}$. $H_{\text{eff}}$ comprises the Hamiltonian $H_{\text{int}}$ as well as the particle-number-conserving terms from the part describing the L and R baths, i.e., the terms proportional to $E_{ij}^{(\alpha)}$ as well as the terms containing the anticommutators in Eq. (4). This deterministic time evolution is interrupted by stochastic jump processes to different particle sectors, mediated by jump operators $L_k^{(\beta)}$, see Appendix A for details. Observables are determined as the average over expectation values in independent realizations of $|\psi\rangle$. Such a stochastic unraveling of the Lindblad equation into a pure state description, in the form of Eq. (11), only works for quantities which only require the knowledge of the time-dependent density matrix $\rho(t)$, as is the case for expectation values $\langle A \rangle = \text{Tr} A(t)\rho = \text{Tr} A\rho(t)$. When evaluating a Greens function, multiple operators at different times are involved and additional information is required. In order to compute two-time correlation functions,

$$G_{BA}(t, t') = \langle \psi(t_0) | B(t) A(t') | \psi(t_0) \rangle, \tag{13}$$

---

**Stochastic wave function (SWF) algorithm**

1. Start with a normalized state $|\psi(t_0)\rangle$ and draw a random number $r_j \in (0, 1)$.

2. Time evolve the state vector with the effective Hamiltonian Eq. A6: $|\psi(t)\rangle = e^{-iH_{\text{eff}}(t-t_0)} |\psi(t_0)\rangle$ up to a time $t_j$ such that $\||\psi(t_j)\rangle\|^2 = r_j$.

3. Perform a quantum jump:

   - Compute the weights for all possible jumps, $w_{\beta k} \propto \|L_k^{(\beta)} \psi(t_j)\|^2$.

   - Select one jump process $(\beta' k')$ at random according to the weights.

   - Change $|\psi(t)\rangle = L_{k'}^{(\beta')} |\psi(t_j)\rangle$ and normalize it.

4. Set $t_0 = t_j$ and iterate $1 \to 4$.

**Single-time observables**

Measure at desired times and average over a sufficient number of realizations $\psi_i(t)$.

$$\langle A(t) \rangle = \frac{1}{n} \sum_{i=1}^{n} \frac{\langle \psi_i(t) | A | \psi_i(t) \rangle}{\|\psi_i(t)\|^2}$$

FIG. 1. The stochastic wave function algorithm for the time evolution.

---

we follow the approach outlined in Ref. [48] and consider the stochastic time evolution of a doubled Hilbert space resulting in the algorithm in Fig. 2.

Here a state vector $|\psi\rangle$ is evolved in time together with a corresponding vector $A|\psi\rangle$. A Green's function is then proportional to the stochastic sample of off-diagonal matrix elements of the second operator $B$, see Eq. (14). Notice that for single-fermion Green's functions, $A$ is a fermionic creation (annihilation) operator. In that case one has to use the negative sign in front of the jump term for the lower part of the doubled Hilbert space, cf. Eq. (A4), see Appendix B in Ref. [64]. Notice that generalizing the doubled Hilbert space to a multiple Hilbert space allows us to sample different correlation functions at once, see Appendix Sec. A 2 b i.

The SWF algorithm requires a routine which is able to time evolve an initial vector with a non-Hermitian generator for some (arbitrarily-) small time $dt$. In the present work we use the so-called Arnoldi algorithm [39] for the time evolution which is the Lanczos method generalized to the non-Hermitian case. For more details, see the Appendix.

## IV. EXTRAPOLATION OF OBSERVABLES TO THE LIMIT OF VANISHING COST FUNCTION

As illustrated above, AMEA is a method which can be systematically improved by increasing the number of bath sites $N_B$ leading to an exponential decrease in the cost function, $\chi = \sum_\alpha \chi_\alpha$, which is a measure of the overall accuracy. Clearly, the best approximation for some quantity of interest
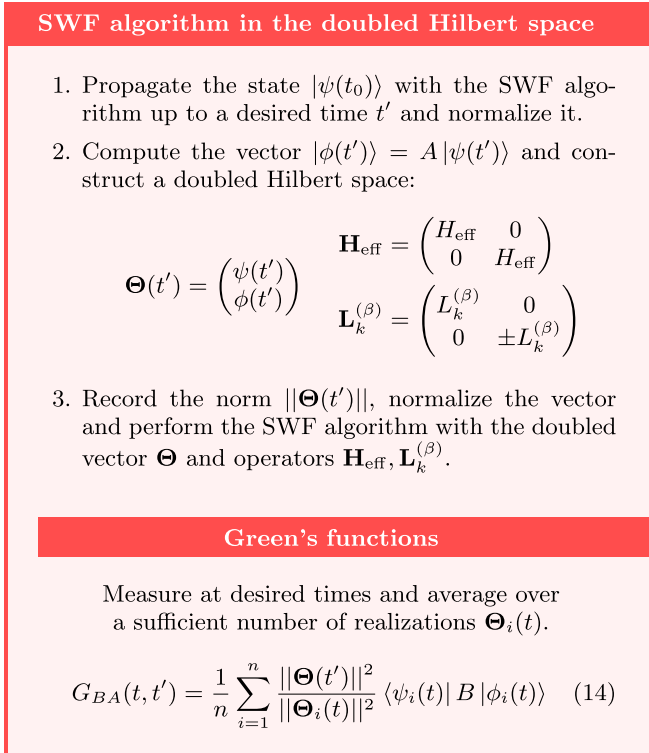
---

**SWF algorithm in the doubled Hilbert space**

1. Propagate the state $|\psi(t_0)\rangle$ with the SWF algorithm up to a desired time $t'$ and normalize it.

2. Compute the vector $|\phi(t')\rangle = A|\psi(t')\rangle$ and construct a doubled Hilbert space:

$$\Theta(t') = \begin{pmatrix} \psi(t') \\ \phi(t') \end{pmatrix} \qquad \mathbf{H}_{\mathrm{eff}} = \begin{pmatrix} H_{\mathrm{eff}} & 0 \\ 0 & H_{\mathrm{eff}} \end{pmatrix}$$

$$\mathbf{L}_k^{(\beta)} = \begin{pmatrix} L_k^{(\beta)} & 0 \\ 0 & \pm L_k^{(\beta)} \end{pmatrix}$$

3. Record the norm $||\Theta(t')||$, normalize the vector and perform the SWF algorithm with the doubled vector $\Theta$ and operators $\mathbf{H}_{\mathrm{eff}}, \mathbf{L}_k^{(\beta)}$.

---

**Green's functions**

Measure at desired times and average over a sufficient number of realizations $\Theta_i(t)$.

$$G_{BA}(t,t') = \frac{1}{n}\sum_{i=1}^{n} \frac{||\Theta(t')||^2}{||\Theta_i(t)||^2} \langle \psi_i(t)| B |\phi_i(t)\rangle \quad (14)$$

FIG. 2. The stochastic wave function algorithm in the doubled Hilbert space which allows us to calculate correlation functions.

for given $N_B$ is obtained within the auxiliary system with the smallest $\chi$. To improve on these results one can think of numerically extrapolating the results to the $\chi \to 0$ limit. This is equivalent to a scaling to the limit of an infinite number auxiliary bath sites $N_B \to \infty$. However, since the accuracy is directly related to $\chi$ rather than $N_B$, it is more convenient to use $\chi$ as an extrapolating parameter. For a given observable $A$ of interest we can assume for its deviation from its exact (physical) value

$$\Delta A(\chi) = A_{\mathrm{ph}} - A_{\mathrm{aux}}(\chi) = k_A \; \chi + O(\chi^2) \quad (15)$$

with some constant of proportionality $k_A$. This suggests that given a series of value pairs $\{\chi_i, A(\chi_i)\}$ one can obtain an approximation to $A_{\mathrm{aux}}(\chi = 0)$ by performing a linear fit in the $(\chi, A)$ plane. Within AMEA a series of value pairs $\{\chi(N_B), A\}$ is naturally generated by the different possible auxiliary system sizes. The truncation of the Taylor series, Eq. (15), to first order is only justified for cost functions which are small compared to $\chi_0 \equiv \chi|_{\Delta_{\mathrm{aux}}=0}$ which is $\chi$ obtained by Eq. (8) with $\Delta_{\mathrm{aux}} = 0$. The resulting normalized cost function, $\chi/\chi_0$, is then a measure for the relative error from the physical situation.

We want to emphasize that the extrapolation scheme presented here is not able to give a consistent error estimate of the extrapolated value as the uncertainty of the individual data points is unknown and not statistically distributed.

Here one has to distinguish between a purely statistical error stemming from the solution of the Lindblad system within stochastic wave functions, which is known and negligible, and the systematic error introduced by the mapping to

the auxiliary system, which is unknown. Further, the role of the higher-order terms in Eq. (15) introduces another source of unknown error. To get a grip on the error due to the AMEA mapping, one could perform the extrapolation in some limit where the true value in the physical system is known, for example, at zero interaction strength or for some other parameters where the value is known from the literature. One could then use the deviation from the extrapolation fit as an approximation to the error of a data point. Since there is a lot of freedom in obtaining this error estimates—and it will thus be very situation dependent—we will not pursue this further in the current work where we are interested in an unbiased benchmark of the extrapolation scheme.

Nevertheless, this scheme provides a significant improvement, for example, in the current, as can be seen in Fig. 5.

## V. APPLICATION TO THE INTERACTING RESONANT LEVEL MODEL

The IRLM [4] is a commonly used nonequilibrium impurity model of spinless fermions. It features an impurity site connected to two semi-infinite tight-binding chains together with an interaction term coupling the particle densities of the impurity site to the neighboring chain sites, see Fig. 3. The Hamiltonian is defined as

$$H_{\mathrm{IRLM}} = H_L + H_R + H_{\mathrm{dot}},$$

$$H_L = -J \sum_{r=-\infty}^{-2} c_r^{\dagger} c_{r+1} + \mathrm{H.c.},$$

$$H_R = -J \sum_{r=1}^{+\infty} c_r^{\dagger} c_{r+1} + \mathrm{H.c.},$$

$$H_{\mathrm{dot}} = -J' \sum_{r=\pm 1} c_r^{\dagger} c_0 + \mathrm{H.c.},$$

$$+ U \sum_{r=\pm 1} \left( c_r^{\dagger} c_r - \frac{1}{2} \right) \left( c_0^{\dagger} c_0 - \frac{1}{2} \right), \quad (16)$$

where $c_r^{\dagger}/c_r$ denote the fermionic creation or annihilation operators at site $r$. Here $H_{L-R}$ describe the semi-infinite tight-binding chains of bandwidth $W = 4J$ and $H_{\mathrm{dot}}$ introduces the hopping to the impurity as well as the interaction term. A nonequilibrium steady-state situation is induced in the system via an applied bias voltage $V$ simulated by shifting the chemical potentials of the leads symmetrically, that is, $\mu_l = -\mu_r = \frac{V}{2}$. We use $J$ as unit of energy and work in units where $\hbar = e = k_B = 1$.

The IRLM is known to be integrable [4] and becomes equivalent to the continuum model in the so-called scaling regime where the bandwidth becomes the largest energy scale in the system. Most notably, there is a closed form expression for the steady-state current as a function of the bias voltage [6,65] for the special value of the interaction $U = 2$,

$$I(V) = \frac{V}{2\pi} {}_2F_3\left[ \left\{ \frac{5}{6}, \frac{7}{6} \right\}, \left\{ \frac{1}{4}, \frac{3}{4}, 1 \right\}; -\left( \frac{V}{V_c} \right)^6 \right], \quad (17)$$

with $V_c = r(J')^{\frac{4}{3}}$ and $r \approx 3.2$ [66]. Here ${}_2F_3(a, b; z)$ is the generalized hypergeometric function [67]. The formula
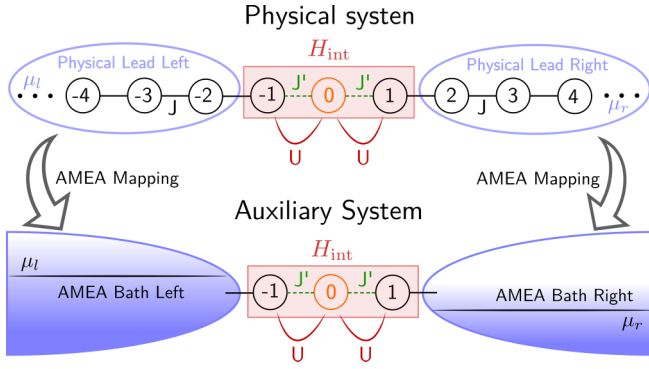
FIG. 3. A sketch of the IRLM as lattice model and its mapping to the auxiliary open quantum system used within AMEA.

Eq. (17) is valid at zero temperature and in the scaling regime. Parameters can be considered to be in the scaling regime [68] if the $I(V)$ function falls onto a single curve in the scaling plot, see Fig. 5. In this way, $I/V_c$ becomes a universal function of the scaled voltage $V/V_c$ alone and in particular does not depend on the hybridization strength $J'$.

### A. AMEA for the IRLM

In the IRLM, the interaction lives on the contact links to the leads and, therefore, the interacting region comprises the sites $r = \{-1, 0, 1\}$ which corresponds to having

$$H_{\text{int}} = H_{\text{dot}}, \tag{18}$$

$$H_{B_L} = -J \sum_{r=-\infty}^{-3} c_r^\dagger c_{r+1} + \text{H.c.}, \tag{19}$$

$$H_{B_R} = -J \sum_{r=2}^{\infty} c_r^\dagger c_{r+1} + \text{H.c.}, \tag{20}$$

$$H_{\text{Hyb}} = -J(c_{-2}^\dagger c_{-1} + c_1^\dagger c_2) + \text{H.c.}, \tag{21}$$

as indicated in Fig. 3. Since $H_{B_{L/R}}$ describe semi-infinite tight-binding chains in equilibrium, $\Delta_{\text{ph},L/R}$ represent baths with a semicircular density of states with a bandwidth of $W = 4$ and an electronic distribution function given by the Fermi function. Within AMEA, a given parameter set $E^\alpha$, $\Gamma^{\alpha,(1,2)}$ fixes both the density of states as well as the distribution function of the corresponding bath. Since the Hamiltonian Eq. (16) is particle-hole symmetric, it suffices to perform
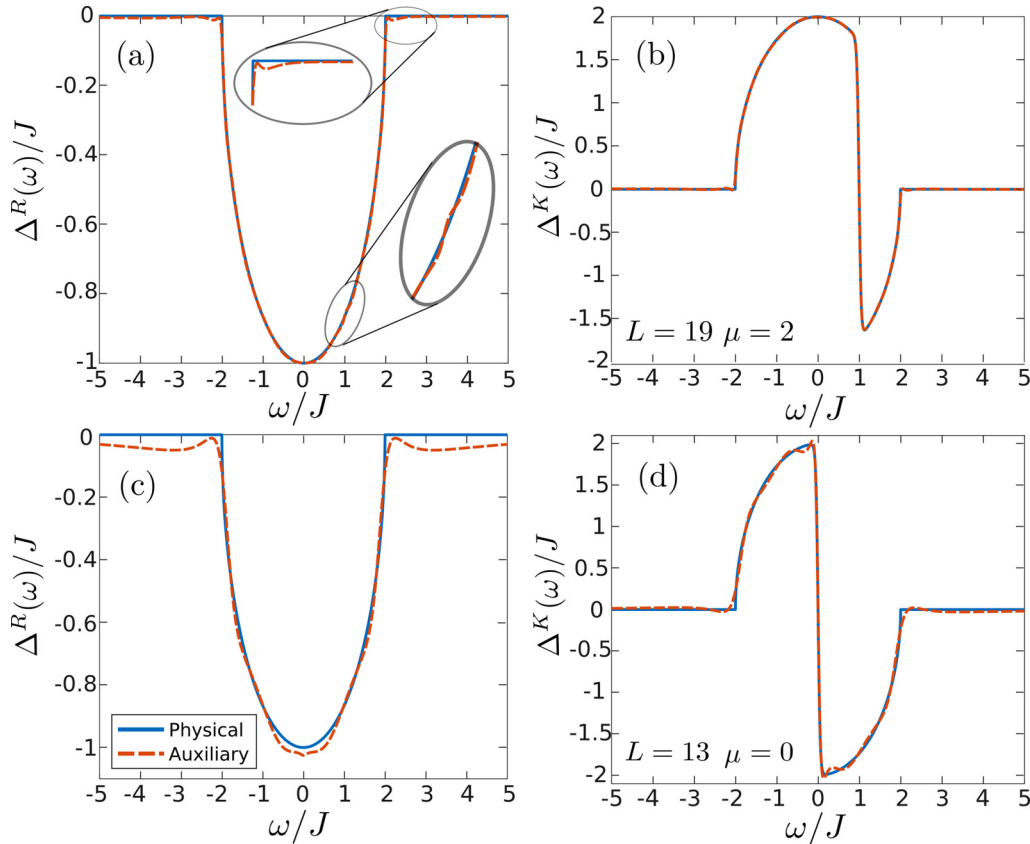


FIG. 4. Comparison of the physical and auxiliary hybridization function at the boundary of the left bath, i.e., $r = -1$, and $T = 0.025$. [(a) and (b)] Retarded-Keldysh part of the hybridization function for $L = 19$, $\mu = 2$. [(c) and (d)] Retarded-Keldysh part of the hybridization for $L = 13$, $\mu = 0$. The $L = 19$ results where obtained with the ADAM routine from Sec. II B 1 while $L = 13$ was optimized with PT. Solid lines represent the hybridization of the physical system, $\Delta_{\text{ph}}$, and dashed lines that of the auxiliary system, $\Delta_{\text{aux}}$. Panels (a) and (b) show a fit for $\mu \neq 0$ to exemplify the capability of representing a nonequilibrium situation. Panels (c) and (d) illustrate the fit used for the calculation of the equilibrium spectral functions in Fig. 6. The insets in panel (a) show a zoom onto the band edge and the region around the chemical potential, $\mu = 1$, where the sudden occupation change in the Keldysh component typically induces oscillations in the retarded one.
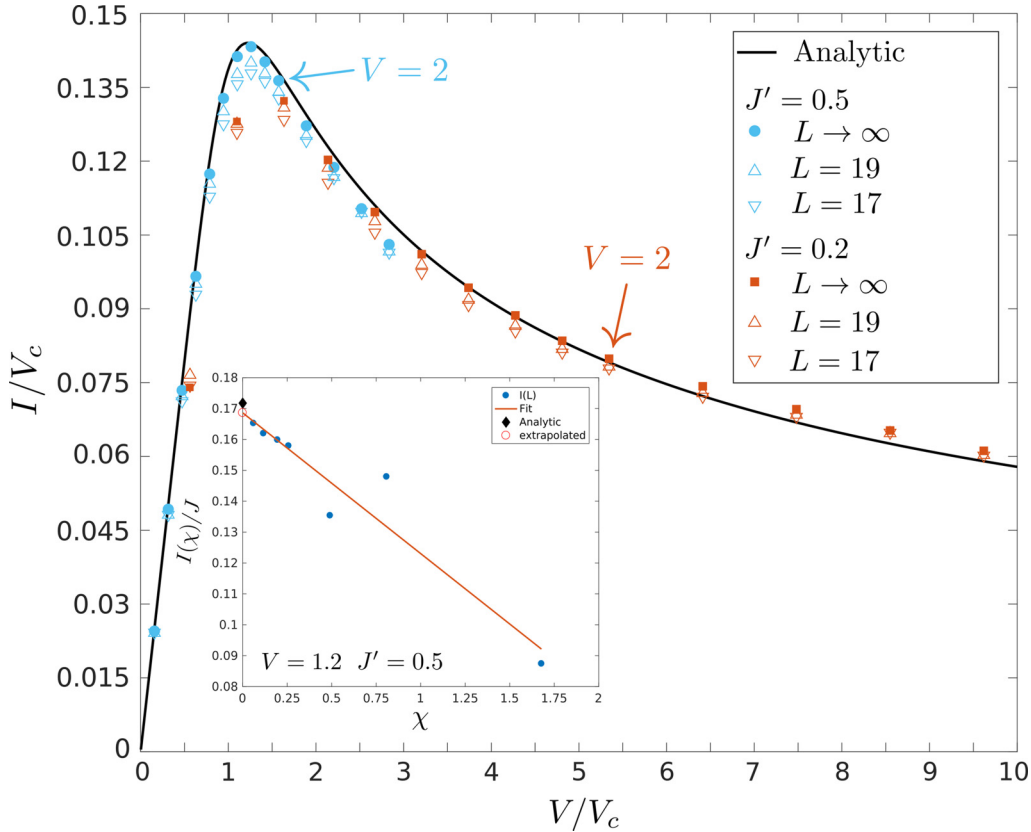
FIG. 5. Scaled steady-state current as function of the scaled bias voltage $V/V_c$. We plot the analytic solution for $T = 0$ (solid black line), the extrapolated AMEA current (filled circles), and the current for $L = 17$ and $L = 19$ (open symbols). Shown are results for $J' = 0.2$ (red symbols) and $J' = 0.5$ (blue symbols). The arrows indicate the data points which correspond to the voltage $V = 2$ for the two different considered $J'$. The inset shows an example of the current vs. cost function $I(\chi)$ for $V = 1.2$, $J' = 0.5$ (filled blue circles) and the corresponding linear fit (solid red line) as well as the extrapolated value at zero cost function (open red circle) together with the analytic result (filled black diamond). Other parameters are $T = 0.025$ and $U = 2$.

the fit only for one of the two baths, e.g., the left ones, and obtain the parameters of the right bath by a particle-hole transformation. Thus, also the cost function for the left and right bath will be equal for a given bias voltage, $\chi_L = \chi_R$. To illustrate the mapping, we show in Fig. 4 two examples for such a fit with $L = 13$ ($N_B = 6$) and $L = 19$ ($N_B = 9$). Notice that the same fit can be used for any set of parameters in the interacting region.

### B. Extrapolation of the steady-state current

Since there are no free parameters in Eq. (17) we can use this as a benchmark for our numerical approach and test the extrapolation scheme of Sec. IV. However, it should be noted that our results are obtained for $T = 0.025$ while Eq. (17) is the result for zero temperature.

Given an auxiliary system of size $L$ we can evaluate the current over a physical bond $i$ in the auxiliary system [69]

$$
\begin{aligned}
I_{i,i+1} &= E_{i+1,i}\langle c_{i+1}^\dagger c_i\rangle - E_{i,i+1}\langle c_i^\dagger c_{i+1}\rangle, \\
&= 2E_{i+1,i}\mathrm{Im}\langle c_{i+1}^\dagger c_i\rangle, \quad\quad (22)
\end{aligned}
$$

where the parameters $E_{i,i+1}$ represent the hopping along the chain in the interacting region. In the following, we consider

results obtained with $7 \leqslant L \leqslant 19$. In Fig. 5 we plot the universal steady-state current together with the corresponding data points obtained with AMEA for $J' = 0.5$ and $J' = 0.2$. Shown are the AMEA results for individual system sizes as well as the extrapolated current. We find a linear relationship to normalized cost functions, $\chi/\chi_0 \approx 1$, suggesting that higher-order terms in the Taylor expansion, Eq. (15), are suppressed in the present case.

We see that the current improves significantly toward the analytic solution thanks to the extrapolation scheme. As mentioned above, the analytic solution is only valid for not-too-large bias voltages [70]. Indeed, we see a systematically growing deviation between the analytic solution and the current from AMEA for voltages $V \gtrsim 2$; see the markers in Fig. 5.

For $J' = 0.2$, somewhat larger deviations from the analytic solution are visible around the maximum of the scaled current. These are due to the finite temperature, which introduces a broadening of the Fermi edge and, thus, can be seen as an uncertainty [71] in the chemical potentials or, equivalently, in the voltage $\Delta V \sim T$. The important point is that this uncertainty is symmetric around the correct $V$ value. In the linear regime, this uncertainty is compensated, because to a $\pm\delta V$ corresponds (approximately) a $\pm\delta I$ which essentially

cancels out. This does not occur in the quadratic regime close to the maximum. Therefore, here the error in $I$ is larger. This effect is larger for small $J'$ because any error in the current gets amplified in the scaling plot for $J' = 0.2$ (where $V_c = \approx 0.37$) in contrast to $J' = 0.5$ (where $V_c \approx 1.27$).

The inset in Fig. 5 shows an example extrapolation. As one would expect, the data points with bigger cost functions (smaller system sizes) show a stronger scattering from the linear fit than the more accurate points. While the points with low cost functions make for more confidence in the results, the accuracy of the extrapolated current does not suffer when the biggest system size, $L = 19$, is excluded from the analysis. This suggests that when utilizing the extrapolation to zero cost function, it is probably not necessary to simulate the biggest system sizes within reach. Rather, one can check for a small fraction of points whether the (usually very CPU-time intensive) bigger system size(s) are worth calculating. However, if error estimates are used, then points at lower cost functions will reduce the uncertainty in the final result.

### C. Spectral function of the IRLM

In this section, we evaluate the steady-state single-particle Green's function $G$ at the central impurity site. The calculation is carried out in the real time domain and we use the approach discussed in Sec. III, see also Sec. A 2. We use a step size of $dt = 0.05$ and $10^5$ time steps to first reach the steady state at $t_0 = 5 \times 10^3$. We have verified that expectation values of static observables do not change after this time. Then we sample the Green's function $G(t - t_0)$ for later times beyond $t_0$ up to $t_{\text{end}} = t_0 + 6000 dt$. This is sufficient, since here $G(t_{\text{end}} - t_0) < 10^{-6}$. Finally, we average $G$ over $O(10^5)$ realizations and determine the spectral function by direct Fourier transform. All results presented in this section are obtained with an auxiliary system of size $L = 13$. The corresponding hybridization function is shown in the lower panels of Fig. 4.

Like any nonequilibrium approach, AMEA is also applicable in equilibrium situations which is just the special case when $\mu_l = \mu_r = 0$, allowing us to compare our results against the literature. In Fig. 6, we compare our results to the equilibrium density of states obtained by Braun and Schmitteckert via MPS [72]. For interaction strengths $U < 2$ that are small compared to the bandwidth, we observe a very good agreement with the reference over the whole frequency range. At the self-dual point $U = 2$ we start to see small quantitative deviations of peak heights but still obtain an satisfactory agreement. When the interaction becomes comparable to the bandwidth, $U = 3$, the deviations become significant and continue to grow as the interaction is increased (not shown). The reason for the growing deviations, such as sharper resonances in the AMEA results and a different behavior around zero frequency, is that in the present AMEA mapping to a system of size $L = 13$ the region outside the bandwidth is not well reproduced, see also Fig. 4. While these states do not play a role as long as all energy scales in the system are small compared to the bandwidth, i.e., in the scaling regime, the details of the leads at higher energies become important when the interaction becomes comparable to the bandwidth. However, the latter does not mean that AMEA is not at all
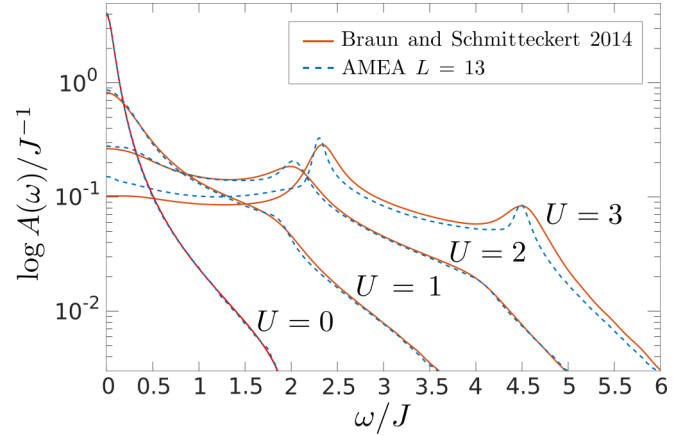


FIG. 6. Equilibrium ($V = 0$) spectral function at the impurity site, $r = 0$, for different interaction strengths. We compare our results with Braun *et al.* [72] (obtained at $T = 0$). Our parameters are $J' = 0.2$, $T = 0.025$.

applicable in this parameter regime; rather, one has to make sure that the region outside the bandwidth is also faithfully reproduced by the auxiliary system. This can be achieved by using a differently distributed cost function in the fit or by going to larger auxiliary system sizes.

#### Impurity spectral function at finite temperatures

We complement our benchmark of the spectral function in the limit of low temperatures with a presentation of finite temperature results, where our method has an even better accuracy. In Fig. 7, we plot the impurity spectral function for increasing temperatures and two different hybridization strengths, $J' = 0.2$ and $J' = 0.5$, at the self-dual point $U = 2$.

We observe that with rising temperature the resonances around $\omega \approx 2, 4$ get weakened and the spectral function develops a broad central peak for both considered hybridization strengths. While for $J' = 0.2$ the amplitude of this peak is decreasing with increasing temperature, the trend is reversed for $J' = 0.5$ where the peak is formed around $T = 0.8$ and continues to grow. This different behaviors can be interpreted as the consequence of two competing effects of the increasing temperature. First, there is a shift of spectral weight away from the resonances around $\omega \approx 2, 4$ to small frequencies which leads to an increase of the central peak. Second, in addition to broadening effects due to the hybridization, the central peak gets broadened by temperature which tends to decrease its height due to the overall normalization.

For the smaller hybridization strength, where the initial broadening due to the hybridization is smaller, the increase in broadening initially dominates over the shift of spectral weight, leading to a decreasing central peak as function of temperature, while the two effects balance out for high temperatures, $T \approx 1$. In the case of the larger hybridization, the shift of spectral weight dominates the behavior of the zero-frequency spectral function.
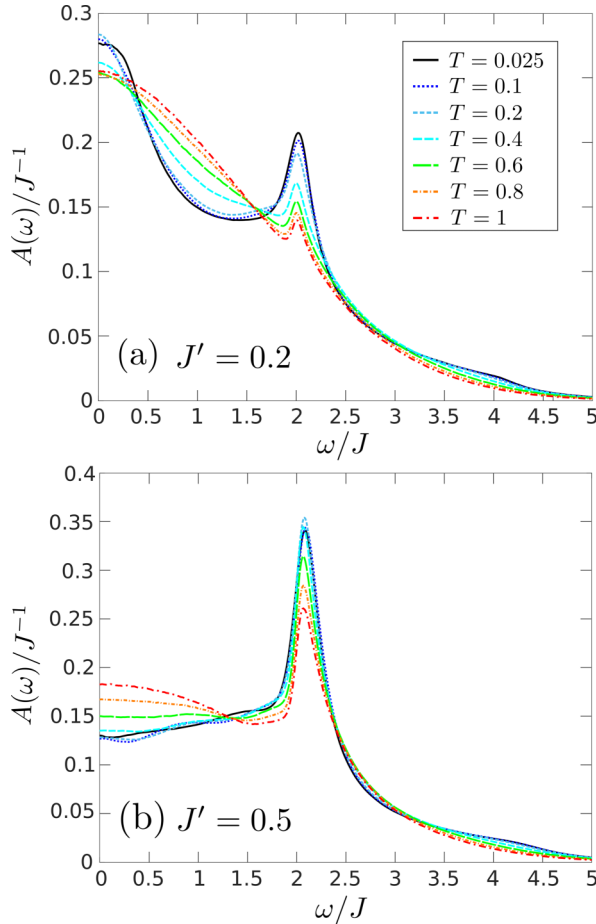
FIG. 7. Equilibrium spectral function at the impurity site, $r = 0$, for different temperatures and two different hybridization strengths. Panel (a) for $J' = 0.2$ and panel (b) for $J' = 0.5$.

### D. Performance

From a numerical point of view, the SWF method has two main advantages. First, since one evolves wave functions there is no need to square the Hilbert space as when one deals with the density matrix. For the present case of using Krylov-space methods, this means that one can use a twice as large $L$ and thus achieve a much better accuracy. Second, individual realizations of possible time evolutions are independent, which means that the method is easily parallelizable. This makes SWF very suitable for future cluster facilities which thrive on highly parallel algorithms.

However, the price to pay is a CPU time that is about 20 times longer than solving an auxiliary system with the same value of the cost function by MPS. On the other hand, thanks to parallelization, the wall time can obviously be made almost arbitrarily small. For example, the GF's for $L = 13$ in Fig. 6 where averaged over about half a million realizations where a single one takes around 1 s. For comparison, the solution with the superfermion plus ED approach for $L = 13$ would be on the order of minutes.

## VI. SUMMARY, CONCLUSION, AND OUTLOOK

We reported on technical developments within the auxiliary master equation approach and applied it to the IRLM

in and out of equilibrium to benchmark the new techniques. We successfully applied the SWF algorithm to determine the steady-state properties of the auxiliary Lindblad system. On the one hand, the SWF algorithm is highly parallelizable allowing to reach very low wall times. On the other hand, we found that in the current implementation of SWF+ED the total CPU time for a spectral function is 20 times higher than in available alternatives for the solution of the auxiliary system introduced by AMEA. Further, we saw that an auxiliary system size of $L = 13$ is enough to obtain reliable spectral information of the IRLM for interactions $U \lesssim W/2$.

We obtained a further significant improvement by extrapolating physical quantities, most notably the current, to the $N_B \to \infty$ limit. In fact, it turns out to be more effective to extrapolate linearly in the cost function $\chi$, which then would correspond to an exponential extrapolation in $N_B$. Such an extrapolation is able to improve the results significantly and possibly circumvents the need to go to larger system sizes.

In addition, we introduced a variable rank parametrization of the auxiliary Lindblad matrices which typically reduces the number of fitting parameters in the AMEA mapping. Employing the new parametrization together with an optimization routine from machine learning, we were able to maintain an exponential decrease of the cost function also for larger system sizes where the previously used parallel tempering algorithm failed.

In view of the high parallelizability of the SWF algorithm, which we found to hold in practice, the fact that MPS is limited in CPU time rather than system size makes a possible SWF+MPS implementaion of AMEA an ideal combination. Especially the combination of AMEA within SWF and FTPS [54]—a generalization of MPS—together with further optimizations, such as extrapolating the Green's function to larger times with linear prediction, could prove to be very fruitful with respect to nonequilibrium DFT+DMFT.

Besides the technical developments within AMEA and their benchmark within the IRLM, we also investigated the effect of increasing temperature on the impurity spectral function. We find that the competition of temperature induces broadening effects and shift of spectral weight gives rise to different behaviors of the spectrum around zero frequency for different hybridization strengths.

### APPENDIX: TECHNICAL DETAILS OF THE SWF ALGORITHM

In order to present the SWF algorithm, we consider a general Lindblad system for a generalized "density-matrix" $\tilde{\varrho} = f(\{c^{(\dagger)}\})\rho$, where $f(\{c^{(\dagger)}\})$ denotes some function of fermionic operators,

$$\mathcal{L} = \mathcal{L}_H + \mathcal{L}_D. \tag{A1}$$

It is composed of a central region with Hamiltonian $H$ and the corresponding Liouvillian $\mathcal{L}_H$,

$$\mathcal{L}_H \tilde{\varrho} = -i[H, \tilde{\varrho}], \tag{A2}$$

and a dissipative part described by $\mathcal{L}_D$,

$$\mathcal{L}_D \tilde{\varrho} = 2 \sum_{ij} \Gamma_{ij}^{(1)} \left( \pm c_j \tilde{\varrho} c_i^\dagger - \frac{1}{2}\{\tilde{\varrho}, c_i^\dagger c_j\} \right)$$
$$+ 2 \sum_{ij} \Gamma_{ij}^{(2)} \left( \pm c_i^\dagger \tilde{\varrho} c_j - \frac{1}{2}\{\tilde{\varrho}, c_j c_i^\dagger\} \right). \tag{A3}$$

Here $i$ and $j$ run over all $L$ sites of the system and $\Gamma^{(1)/(2)}$ are $L \times L$ matrices. The minus sign in Eq. (A3) is valid if $\tilde{\varrho}$ is odd in the number of fermion operators, i.e., $\tilde{\varrho} = c_i^{(\dagger)}\rho$. This is the case with Green's functions, where we need to propagate $c_i^{(\dagger)}\rho$.

In order to obtain the jump operators one has to diagonalize the matrices $\Gamma^{(\beta)}$, $\beta = 1, 2$,

$$2\Gamma_{ij}^{(\beta)} = \sum_k U_{ik}^{(\beta)} \gamma_k^{(\beta)} U_{jk}^{(\beta)*},$$

and end up with the eigendecomposition of the dissipator,

$$\mathcal{L}_D \rho = \sum_{\beta k} \left( \pm L_k^{(\beta)} \rho L_k^{(\beta)\dagger} - \frac{1}{2}\{\rho, L_k^{(\beta)\dagger} L_k^{(\beta)}\} \right), \tag{A4}$$

$$L_k^{(1)} = \sum_i \sqrt{\gamma_k^{(1)}} U_{ik}^{(1)*} c_i,$$

$$L_k^{(2)} = \sum_i \sqrt{\gamma_k^{(2)}} U_{ik}^{(2)} c_i^\dagger. \tag{A5}$$

The anticommutators in Eq. (A4) are included into the effective, non-Hermitian Hamiltonian [73],

$$H_{\text{eff}} = H - \frac{i}{2} \sum_{\beta k} L_k^{(\beta)\dagger} L_k^{(\beta)}$$
$$= H - i \sum_{ij} \left[ \Gamma_{ij}^{(1)} - \Gamma_{ij}^{(2)} \right] c_i^\dagger c_j - i \sum_i \Gamma_{ii}^{(2)}. \tag{A6}$$

With this Hamiltonian and the jump operators $L_k^{(\beta)}$, Eq. (A5), one formulates the SWF algorithms in Sec. III, Figs. 1 and 2.

### 1. Jump-time search and Arnoldi

As mentioned in Sec. III we use the so-called Arnoldi algorithm [39] for the time evolution. Arnoldi is a Krylov space method analog to Lanczos but for non-Hermitian Hamiltonians. For a given initial state, $|\psi_0\rangle$, and time interval, $dt$, a Krylov space, spanned by $Q$, is generated by iteratively

applying $H_{\text{eff}}$ to the starting vector until a satisfactory approximation for the time evolution operator $e^{-iH_{\text{eff}}dt} \approx Q^\dagger e^{-iH_K dt} Q$ is found. For any given time $t$ up to the maximal time $dt$, the state and the corresponding norm needed for the SWF algorithm are given by

$$|\psi(t)\rangle = Q^\dagger e^{-iH_K t} Q |\psi_0\rangle = Q^\dagger e^{-iH_K t} \vec{v}_0, \tag{A7}$$

$$\vec{v}_0 = Q|\psi_0\rangle = (1, 0, 0, \dots)^\top, \tag{A8}$$

$$\|\psi(t)\|^2 = \langle \psi_0 | Q^\dagger e^{iH_K^\dagger t} \underbrace{QQ^\dagger}_{\mathbb{1}} e^{-iH_K t} Q |\psi_0\rangle, \tag{A9}$$

$$= \vec{v}_0^\top e^{iH_K^\dagger t} e^{-iH_K t} \vec{v}_0, \tag{A10}$$

where we have used the property that $Q|\psi_0\rangle$ is nothing else than the first Krylov vector and $QQ^\dagger = \mathbb{1}$ is the identity [74]. We want to point out that by virtue of Eq. (A10) the norm can be calculated within the Krylov space representation itself, which is typically of size $\dim_K = O(10)$, without the need to use the transformation matrices $Q$ which are of dimension $\dim_Q = \dim_F \dim_K$, where $\dim_F$ is the dimension of the Hilbert space (many-body Fock space). Differentiating Eq. (A10) yields

$$\frac{d}{dt}\|\psi(t)\|^2 = -2\text{Im}\left( \vec{v}_0^\top e^{iH_K^\dagger t} i H_K e^{-iH_K t} \vec{v}_0 \right), \tag{A11}$$

which allows to determine the jump time $t_j$ in the SWF algorithm, satisfying $\|\psi(t_j)\|^2 - r_j = 0$, by applying Newton's method.

### 2. Practical implementation for the steady-state situation

Here we want comment on the practical implementation for the special case of steady-state quantities.

#### a. Steady-state observables

We start with the, with respect to the needed numerical simulation protocol, simpler case of sampling a steady-state observable. A steady-state expectation value is obtained like in a MC simulation. We start with a random starting state and time evolve the system until it reaches the steady state, where the system is time-translational invariant (like the thermalization in a MC simulation). Once we are in the steady state, we start measuring the observable generating an autocorrelated time series from which an estimator of the expectation value can be obtained. As usual the time series needs to be long enough to have overcome autocorrelations, which can be checked for example by a Binning plot.

For the present case we typically recorded $N_m = 2^{18}$ measurements separated by a time $\Delta t = N_{t_{\text{skip}}} dt$ with a time step $dt = 0.05$ and $N_{t_{\text{skip}}} dt = 16 dt \approx 10 \bar{t}_j$, where $\bar{t}_j$ is the average jump time. For thermalization we performed additionally 10% of the total time evolution leading to $O(10^5)$ thermalization time steps. Parallelization can be achieved by computing several individual realizations on a single cluster node, where each realization is bound to one core, for instance.

#### b. Steady-state single-particle GF's

To obtain steady-state GF's of the Lindblad system we follow Ref. [40]. In short, it is best to calculate the lesser and

greater steady-state GF, defined by

$$G_{ij}^<(t) = i\langle c_i^\dagger(t)c_j\rangle_\infty, \quad G_{ij}^>(t) = -i\langle c_i(t)c_j^\dagger\rangle_\infty, \quad (A12)$$

where $\langle \cdot \rangle_\infty = T_r\{\cdot \rho_\infty\}$ denotes the expectation value in the steady state. We sample the GF by first time evolving into the steady state like above. Next, we apply the operator $c_r^{(\dagger)}$, construct the doubled Hilbert space, continue to time evolve in the doubled Hilbert space, and measure according to the SWF algorithm in the doubled Hilbert space.

As stated in the main text, the time steps needed for GF's is of $O(10^3)$ and to reach the accuracy needed for smooth spectral functions, we had to average over $O(10^5)$ realizations. Further, we perform $O(10^5)$ time steps to get into the steady state. For the performance in terms of CPU time, it is crucial that the time steps into the steady state are done only for a small fraction of the realizations; the corresponding final states are saved [75]. Another realization starts from a state obtained by time evolving such a saved state for some time $\Delta t \approx 100 \bar{t}_j$, where $\bar{t}_j$ denotes the mean jump time [76], to make sure that individual realizations are independent to a very good approximation. Here we note that only early times will be correlated as the realizations gain in independence through the jumps in the time evolution [77].

*i. Multistates.* One can sample multiple correlation functions, $G_{B_i A_i}(t, t')$, together when generalizing the doubled Hilbert space to a multiple Hilbert space. For this, generalize

$$\Theta(t) = \begin{pmatrix} \psi(t) \\ \phi_1(t) \\ \cdot \\ \cdot \\ \cdot \\ \phi_n(t) \end{pmatrix} \quad (A13)$$

with the excited states $\phi_i = A_i |\psi\rangle$. For instance, this allows us to sample the lesser and greater GF together in a tripled Hilbert space or multiple components of a cluster GF [78],

$G_{ij}$. The advantage is that $|\psi\rangle$ is only time evolved ones, where as in the individual approach, with only a doubled Hilbert space, $|\psi\rangle$ is time evolved $n$ times.

*ii. Destroyed states in the multiple Hilbert space.* Here we want to elaborate on the fact that part of the state may be destroyed when applying the SWF algorithm in the multiple Hilbert space. For simplicity, we consider in the following a doubled Hilbert space. Part of the state can get destroyed when the system leaves the physical particle sectors through the application of a jump operator [79]. For instance, a state can get destroyed when the system is in the $N = L$ particle sector and a jump operator $L_k^{(2)}$ gets chosen that increases the particle number.

First, let us note that this cannot happen in the single Hilbert space since the corresponding weight $w_{\beta k} \propto ||L_k^{(2)}\psi(t_j)||^2$ is zero and this jump operator will never be chosen. The situation is different in the doubled Hilbert space when the two components of a state reside in different particle sectors. Too see this, let us consider the case of the greater GF. Here, if $|\psi\rangle$ is in sector $N$, then $|\phi\rangle$ will always describe a state with $N + 1$ particles, since the jump operator applied is the same for both components. If at some time $t_{\text{kill}}$, $|\phi\rangle$ is in the sector $L$, then the weight for a jump operator that increases the particle number, $w_{\beta k} \propto ||L_k^{(2)}\psi(t_j)||^2 + ||L_k^{(2)}\phi(t_j)||^2$, might be nonzero since the first part can be nonvanishing.

If part of the state is destroyed, then all subsequent measurements in this specific realization of the time series for the GF will all be zero.

It is important to realize that this is the correct behavior. It exemplifies why the doubled Hilbert space is needed when calculating correlation functions and why it would be wrong to simply consider an independent time evolution for the excited state and the initial state separately. In fact, in the independent approach, any correlation between the initial state and the final state would be lost very quickly through the stochastic process and it is key that the two states always jump together, thereby mediating the correlation.

---

[1] P. W. Anderson, Phys. Rev. **124**, 41 (1961).

[2] T. Holstein, Ann. Phys. **8**, 7325 (1959).

[3] J. Kondo, Prog. Theor. Phys. **32**, 37 (1964).

[4] P. Wiegmann and A. Finkelshtein, J. Exp. Theor. Phys. **48**, 102 (1978).

[5] A. C. Hewson, *The Kondo Problem to Heavy Fermions* (Cambridge University Press, Cambridge, 1993).

[6] E. Boulat, H. Saleur, and P. Schmitteckert, Phys. Rev. Lett. **101**, 140601 (2008).

[7] D. Goldhaber-Gordon, J. Göres, M. A. Kastner, H. Shtrikman, D. Mahalu, and U. Meirav, Phys. Rev. Lett. **81**, 5225 (1998).

[8] W. Metzner and D. Vollhardt, Phys. Rev. Lett. **62**, 324 (1989).

[9] M. Eckstein, A. Hackl, S. Kehrein, M. Kollar, M. Moeckel, P. Werner, and F. Wolf, Eur. Phys. J.: Spec. Top. **180**, 217 (2009).

[10] P. Schmidt and H. Monien (unpublished).

[11] A. V. Joura, J. K. Freericks, and T. Pruschke, Phys. Rev. Lett. **101**, 196401 (2008).

[12] M. Eckstein, M. Kollar, and P. Werner, Phys. Rev. Lett. **103**, 056403 (2009).

[13] M. Eckstein, M. Kollar, and P. Werner, Phys. Rev. B **81**, 115131 (2010).

[14] S. Okamoto, Phys. Rev. Lett. **101**, 116807 (2008).

[15] C. Aron, G. Kotliar, and C. Weber, Phys. Rev. Lett. **108**, 086401 (2012).

[16] J. E. Han, Phys. Rev. B **75**, 125122 (2007).

[17] J. E. Han and R. J. Heary, Phys. Rev. Lett. **99**, 236808 (2007).

[18] A. Dirks, P. Werner, M. Jarrell, and T. Pruschke, Phys. Rev. E **82**, 026701 (2010).

[19] C. Aron, C. Weber, and G. Kotliar, Phys. Rev. B **87**, 125113 (2013).

[20] P. Mehta and N. Andrei, Phys. Rev. Lett. **96**, 216802 (2006).

[21] F. B. Anders, Phys. Rev. Lett. **101**, 066804 (2008).

[22] Y. Meir and N. S. Wingreen, Phys. Rev. Lett. **68**, 2512 (1992).

[23] H. Schoeller and G. Schön, Phys. Rev. B **50**, 18436 (1994).

[24] A. Rosch, J. Paaske, J. Kroha, and P. Wölfle, J. Phys. Soc. Jpn. **74**, 118 (2005).

[25] H. Schoeller, Eur. Phys. J.: Spec. Top. **168**, 179 (2009).

[26] S. R. White and A. E. Feiguin, Phys. Rev. Lett. **93**, 076401 (2004).

[27] A. J. Daley, C. Kollath, U. Schollwöck, and G. Vidal, J. Stat. Mech. (2004) P04005.

[28] T. Prosen and M. Znidaric, J. Stat. Mech. (2009) P02035.

[29] F. B. Anders and A. Schiller, Phys. Rev. Lett. **95**, 196801 (2005).

[30] S. Kehrein, Phys. Rev. Lett. **95**, 056602 (2005).

[31] R. Gezzi, T. Pruschke, and V. Meden, Phys. Rev. B **75**, 045324 (2007).

[32] S. G. Jakobs, V. Meden, and H. Schoeller, Phys. Rev. Lett. **99**, 150603 (2007).

[33] C. Jung, A. Lieder, S. Brener, H. Hafermann, B. Baxevanis, A. Chudnovskiy, A. Rubtsov, M. Katsnelson, and A. Lichtenstein, Ann. Phys. **524**, 49 (2012).

[34] F. Chen, G. Cohen, and M. Galperin, arXiv:1810.10509.

[35] E. Arrigoni, M. Knap, and W. von der Linden, Phys. Rev. Lett. **110**, 086403 (2013).

[36] A. Dorda, M. Nuss, W. von der Linden, and E. Arrigoni, Phys. Rev. B **89**, 165105 (2014).

[37] A. Dorda, M. Sorantin, W. von der Linden, and E. Arrigoni, New J. Phys. **19**, 063005 (2017).

[38] A. A. Dzhioev and D. S. Kosov, J. Chem. Phys. **134**, 044121 (2011).

[39] M. Knap, E. Arrigoni, W. von der Linden, and J. H. Cole, Phys. Rev. A **83**, 023821 (2011).

[40] A. Dorda, M. Ganahl, H. G. Evertz, W. von der Linden, and E. Arrigoni, Phys. Rev. B **92**, 125145 (2015).

[41] D. M. Fugger, A. Dorda, F. Schwarz, J. von Delft, and E. Arrigoni, New J. Phys. **20**, 013030 (2018).

[42] I. Titvinidze, A. Dorda, W. von der Linden, and E. Arrigoni, Phys. Rev. B **92**, 245125 (2015).

[43] A. Dorda, I. Titvinidze, and E. Arrigoni, J. Phys.: Conf. Ser. **696**, 012003 (2016).

[44] I. Titvinidze, A. Dorda, W. von der Linden, and E. Arrigoni, Phys. Rev. B **96**, 115104 (2017).

[45] I. Titvinidze, M. E. Sorantin, A. Dorda, W. von der Linden, and E. Arrigoni, Phys. Rev. B **98**, 035146 (2018).

[46] G. Kotliar, S. Y. Savrasov, K. Haule, V. S. Oudovenko, O. Parcollet, and C. A. Marianetti, Rev. Mod. Phys. **78**, 865 (2006).

[47] J. Dalibard, Y. Castin, and K. Mølmer, Phys. Rev. Lett. **68**, 580 (1992).

[48] H.-P. Breuer, B. Kappler, and F. Petruccione, Phys. Rev. A **56**, 2334 (1997).

[49] H. Breuer, B. Kappler, and F. Petruccione, Eur. Phys. J. D **1**, 9 (1998).

[50] For simplicity we neglect spin.

[51] Here it is worth noting that the matrices $E^{(\alpha)}$, $\Gamma^{(\alpha),1}$, $\Gamma^{(\alpha),2}$ are only nonzero in the part of the system which describes the corresponding bath.

[52] We stress that for fixed total number of bath sites the accuracy of AMEA is comparable to the one of the equilibrium ED solver [80] with more than twice as many bath sites. This is because for fixed $N_B$ AMEA offers more than twice as many fit parameters, $E$, $\Gamma^{(1)}$, $\Gamma^{(2)}$, than equilibrium ED, which is parametrized by a single matrix, $E$.

[53] This is the time it takes to obtain a given result. The wall time can be much smaller than the CPU time for a highly parallelized algorithm.

[54] D. Bauernfeind, M. Zingl, R. Triebl, M. Aichhorn, and H. G. Evertz, Phys. Rev. X **7**, 031013 (2017).

[55] D. Bauernfeind, R. Triebl, M. Zingl, M. Aichhorn, and H. G. Evertz, Phys. Rev. B **97**, 115156 (2018).

[56] Although it is desirable, as it gives the best approximation for a given system size.

[57] This corresponds to the case $N_B > 6$ when allowing for the most general Lindblad couplings.

[58] For example, we observed that for a system with $N_B = 9$ bath sites, increasing rank$_\gamma > 4$ was not fruitful in terms of the cost function.

[59] D. P. Kingma and J. Ba, arXiv:1412.6980.

[60] M. Abadi, A. Agarwal, P. Barham, E. Brevdo, Z. Chen, C. Citro, G. S. Corrado, A. Davis, J. Dean, M. Devin, S. Ghemawat, I. Goodfellow, A. Harp, G. Irving, M. Isard, Y. Jia, R. Jozefowicz, L. Kaiser, M. Kudlur, J. Levenberg, D. Mané, R. Monga, S. Moore, D. Murray, C. Olah, M. Schuster, J. Shlens, B. Steiner, I. Sutskever, K. Talwar, P. Tucker, V. Vanhoucke, V. Vasudevan, F. Viégas, O. Vinyals, P. Warden, M. Wattenberg, M. Wicke, Y. Yu, and X. Zheng, TensorFlow: Large-scale machine learning on heterogeneous systems (2015), available at http://tensorflow. org/.

[61] To be consistent with quantum mechanics, $P[\vec{\psi}, t]$ must not depend on the phase of the wave function and it is only nonvanishing for normalized states.

[62] More generally, $\lambda$ indexes a complete set of quantum numbers.

[63] $P[\vec{\psi}, t]D\vec{\psi}D\vec{\psi}^*$ can then be interpreted as the probability to find the system within the volume element $D\vec{\psi}D\vec{\psi}^*$ around the state $\vec{\psi}$ at time $t$.

[64] F. Schwarz, M. Goldstein, A. Dorda, E. Arrigoni, A. Weichselbaum, and J. von Delft, Phys. Rev. B **94**, 155142 (2016).

[65] S. T. Carr, D. A. Bagrets, and P. Schmitteckert, Phys. Rev. Lett. **107**, 206801 (2011).

[66] In more detail, $V_c = \frac{\sqrt{3}}{4^{2/3}} \frac{4\sqrt{\pi}\Gamma(2/3)}{\Gamma(1/6)} T_B$ and $T_B = c(J')^{\frac{4}{3}}$ with $c \approx 2.7$ from [6].

[67] In contrast to previous works [65,81], we use the standard notation of the generalized hypergeometric function, that is, two arguments first than three.

[68] From previous works [70], we know that at $U = 2$ one has to restrict to $J' \lesssim 0.5$ and $V \lesssim 2$ to be in the scaling regime.

[69] In practice, we measure at all physical bonds and average accordingly. There is a tiny breaking of current conservation due to the numerics.

[70] K. Bidzhiev and G. Misguich, Phys. Rev. B **96**, 195117 (2017).

[71] This is a physical effect and not related to our approximation made within AMEA.

[72] A. Braun and P. Schmitteckert, Phys. Rev. B **90**, 165112 (2014).

[73] For this generalize $[H, \rho]$ to $H_{\text{eff}}\rho - \rho H_{\text{eff}}^\dagger$.

[74] Note that for non-Hermitian problems $Q^\dagger Q \neq \mathbb{1}$.

[75] In the present case the time steps into the steady state make for about 10% of the total run time.

[76] The time between consecutive jumps.

[77] One can test for autocorrelations when considering the different realizations for a specific (early-) time step as a time series and apply autocorrelation analysis.

[78] A matrix of GF's corresponding to a cluster of multiple sites.

[79] Naturally, this happens more often in smaller systems.

[80] M. Caffarel and W. Krauth, Phys. Rev. Lett. **72**, 1545 (1994).

[81] C. Schiegg, M. Dzierzawa, and U. Eckern, New J. Phys. **17**, 083060 (2015).